



# Implementation and virtual assessment of a non-uniform cylindrical slicing algorithm for robot-based additive manufacturing

Jacopo Lettori<sup>1,2</sup> · Roberto Raffaeli<sup>3</sup> · Milton Borsato<sup>2</sup> · Margherita Peruzzini<sup>4</sup> · Marcello Pellicciari<sup>3</sup>

Received: 30 January 2024 / Accepted: 1 February 2024

© The Author(s), under exclusive licence to Springer-Verlag London Ltd., part of Springer Nature 2024

## Abstract

Robot-based additive manufacturing (RBAM) is an additive manufacturing (AM) technology powered by robotic manipulators. The material is deposited from a nozzle onto an initial surface, adding successive layers on top of each other and pouring it along multiple directions (multiaxial deposition) thanks to the dexterity of robots, often of the anthropomorphic type. Furthermore, it is possible to manufacture layers of non-uniform thickness, thus obtaining non-parallel and non-planar layers. In particular, RBAM can be implemented to realize revolved parts with protruding portions. Cylindrical or conical slicing algorithms have been devised to process the sub-volumes, reducing the number of layers and the need for support structures. In this context, the paper presents a novel algorithm for non-uniform cylindrical slicing that processes sub-volumes connected to a cylindrical shape. The specific contribution of the work is an algorithm that moves from a curved slicing to increase the adhesion between the central body and the first layer, and it relaxes the curvature in the subsequent layers, arriving, if possible, at a planar slicing. The algorithm considers robots' intrinsic constraints on movements. Planar paths are better approximated than non-planar ones since they prevent the robot from constantly changing the nozzle angle, thus increasing the overall quality of the printing. The algorithm is applied to four test cases and compared with other slicing approaches using numeric indices, objectivating its strengths and limits.

**Keywords** Robot-based additive manufacturing · Non-planar slicing · Cylindrical slicing · Non-uniform slicing

## 1 Introduction

The execution of a standard additive manufacturing (AM) process traditionally begins with finding a fixed optimal build orientation of an input geometry [1]. Then, the geometry is sliced to obtain successive curves representing the paths the deposition means to manufacture the layers. Planar uniform slicing with a constant layer thickness approach is

mainly implemented in commercial computer-aided manufacturing software due to its simplicity, efficiency, and compliance with the architecture of 3D printers. In this case, the geometric model is intersected by successive equidistant planes along the machine Z + axis, generating a series of curves (or polylines if the input geometry is a polygonal mesh), which form the borders of the single layers to be filled. The distance between the planes corresponds to the layer height. Several algorithms have been optimized to increase efficiency [2, 3]. However, a significant drawback of this approach is represented by the staircase effect generated for processed surfaces that are tilted concerning the slicing direction, degrading the surface finish of the final product [4].

Adaptive planar slicing was developed to overcome the limitations of uniform planar slicing [5]. In this context, the layer thickness varies according to the shape of the processed CAD geometry [6], balancing the staircase effect with the manufacturing time [7]. As different layer heights must be obtained, the process parameters are adapted

✉ Jacopo Lettori  
jacopo.lettori@unimore.it

<sup>1</sup> Department of Engineering “Enzo Ferrari”, Università Degli Studi Di Modena E Reggio Emilia, Via Vivarelli 10, 41125 Modena, Italy

<sup>2</sup> Universidade Tecnológica Federal Do Paraná, Campus Curitiba, Curitiba, Paraná, Brazil

<sup>3</sup> Department of Sciences and Methods for Engineering, Università Degli Studi Di Modena E Reggio Emilia, Via Amendola 2, 42122 Reggio Emilia, Italy

<sup>4</sup> Department of Industrial Engineering, University of Bologna, Viale Risorgimento 2, Bologna, Italy

considering the maximum and minimum thickness that can be manufactured with the selected technology.

Furthermore, adopting a fixed slicing direction with planar uniform or adaptive slicing leads to suspended geometry regions where support structures are required. Support structures increase the manufacturing time, total cost, and material waste, lowering the surface finish [8]. Also, these structures must be removed by a physical, chemical, or thermal process, and this post-processing phase can damage the final product.

Considering these aspects, robot-based additive manufacturing (RBAM) is emerging to increase manufacturing flexibility and guarantee much more extensive build volumes than standard Cartesian AM with 3 degrees of freedom (DoFs) [4]. Directed energy deposition [9] or material extrusion [10] technologies are combined with manipulators and working tables with one or more DoFs [11], enabling the material deposition along multiple directions [12, 13]. Also, non-planar [14] and non-uniform [15, 16] slicing can be adopted with RBAM. These approaches can reduce the total number of layers, the support volume, and the manufacturing time, increasing the final product's quality and mechanical performance [17].

In particular, non-uniform slicing refers to non-parallel planar layers as the slicing direction is changed at each layer [15]. This strategy is achieved by continuously varying the slicing direction following the development of the input geometry. To this aim, the geometrical concepts known as the medial axis [18] and centroid axis [19] can be used to derive dorsal curves for slicing and defining curved trajectories. However, extremal or bulky portions are often not captured [4].

Only some strategies have been devised in the literature to obtain non-planar slicing [20]. In these cases, the input geometry is intersected with a series of non-planar surfaces to get the border curves of the slices [21]. However, strategies that combine non-uniform and non-planar slicing have been marginally studied [14]. Attempts of non-planar slicing are cylindrical [22] or conical [23] slicing approaches used when bosses are to be realized respectively on a cylindrical or conical hub. At first, the initial geometry is divided into the central revolved and connected parts [22, 24]. The slicing curves are then obtained by intersecting the identified overhangs with a series of offsets of the central cylindrical or conical surface [23]. Nonetheless, non-uniform cylindrical or conical slicing strategies still need to be explored.

From a technological point of view, in RBAM, the intrinsic limitations of open kinematic manipulators strongly condition the process. The movements imposed on the robot end effector in the deposition process could lead to the so-called singularities, i.e., configurations in which the robot joint angles are not unique and would require undefined speed to be passed through. Such singularities must be avoided

[25]. Furthermore, in the extended workspace provided by 6 DoFs articulated arms, or even more if positioning tables are adopted, collisions of the depositing means with the part of the devices themselves are always possible. Finally, it must be observed that slicing can be discretized into linear segments to develop a correct and robust instruction file to drive the robot movements [26], transforming a continuous curve into a sequence of segments. The resulting polyline constitutes the robot's path and presents discontinuity in velocity due to differently oriented tangent vectors of the single segments [27]. As a result, the robot must slow down, or even stop, at each point of the polyline, and this phenomenon strongly affects the smoothness of the motion and a regular deposition speed [28]. In general, continuous paths can be achieved only with smoothing functions implemented in the robot controller. In this context, corners are replaced with fillet curves [26]. However, these approximations change the original paths, modifying the visited locations. Scarce documentation about the implemented smoothing functions and actual robot behavior can be found. Finally, the possibility of encountering path discontinuities and robot singularities is augmented in three-dimensional non-planar layers.

In this context, this paper presents a specific non-uniform slicing approach to be applied to parts made of sub-volumes (SVs) connected to a central cylindrically shaped body. In the context of RBAM, the aim is to demonstrate how adopting a proper geometrical processing strategy, i.e., non-planar and non-uniform slicing, can improve the quality of the obtained parts. In particular, the algorithm relies on a transition from curved slicing to a planar one. This way, greater adhesion between the central body and the deposited SVs is initially guaranteed than multiaxial planar slicing [29]. Then, the layer surface curvature is relaxed when no longer needed. So, the proposed approach aims to maximize the smoothness of the robot paths, reducing the possibility of discontinuities and joint singularities compared to pure cylindrical slicing approaches. Furthermore, the proposed approach is framed in the context of a reference framework, whose objective is the definition of a generic geometry processing procedure addressing and assessing the advantages and limitations of a particular RBAM strategy.

The algorithm was developed in Rhinoceros 3D® [30] using the Grasshopper® plug-in for visual programming. Then, generated deposition paths were exported in a robot programming and simulation environment, i.e., RoboDK® [31], to test the feasibility of the generated paths. Four geometries were processed with the proposed algorithm, comparing it with the uniform cylindrical slicing approach and the multiaxial planar uniform slicing. Finally, the algorithms were evaluated using indices to objectivate the slicing results.

The remainder of the paper is organized as follows. The state of the art of non-planar slicing algorithms is reported

in Section 2, focusing on cylindrical shapes. The proposed approach for non-uniform cylindrical slicing is outlined in Section 3 according to a general research framework. The application of the algorithm to the test cases is presented in Section 4. A discussion of the obtained results and the robot path simulation are reported in Section 5. Finally, conclusions and future works are presented in Section 6.

## 2 Background on non-planar and non-uniform slicing

Considering a generic volume to be manufactured through an additive process, it is possible to identify a top surface and a bottom one of the input geometry, as depicted in Fig. 1.

In the literature, a series of non-planar surfaces are intersected with a CAD model in references [20, 21] to generate non-planar slicing curves. Non-planar layers can also be obtained by offsetting the bottom surface facets of an STL model along their normal directions [33], obtaining a cutting surface. This process is repeated from one offset surface to the next until the CAD model is sliced with curved layers, possibly implementing adaptive approaches to increase the surface finish [17]. Nevertheless, self-intersection of triangles can occur while offsetting [4, 34].

Alternatively, curved layers have been obtained by discretizing the space into a regular voxel grid and assuming that material accumulation during the deposition is performed by adding voxels one by one [35]. The computed sequence of voxel accumulation indicates the flow of fabrication. A feasible growing field is calculated with a greedy schema, i.e., an optimal search approach, considering defined constraints. This method claims to reduce the need for support structures. Recently, non-planar slicing has been applied to the top surface [36] and the top and bottom surface [32] (Fig. 1c). In particular, the top and bottom surfaces are sliced with a non-planar strategy, while the central body is sliced with a uniform planar slicing algorithm. These algorithms

have been developed to increase the realized part's surface finish [37].

Few non-planar slicing algorithms implement a non-uniform layer distribution [14, 38]. For example, in recent works, the slicing surfaces have been obtained by analyzing the part shape [39] or recurring to isothermal surfaces computed from heat transfer simulations [40]. Generally speaking, non-uniform and non-planar slicing algorithms are proven to be able to increase, even if on basic geometries, the surface finish, the geometry accuracy, and the mechanical properties of the final part.

Cylindrical and conical slicing algorithms are unique non-planar slicing approaches used when a revolved part around a central axis presents projecting portions. Indeed, overhangs can be sliced by intersecting them with successive offsets of the central surface of the revolved part, thus, obtaining non-planar curves. These curves can be optionally infilled with a particular scheme. RBAM is gaining high interest in realizing such geometries compared to subtractive or forming manufacturing, especially for small production batches. Indeed, RBAM can reduce the material waste and the total cost of the final product [41] as these parts have a high buy-to-fly ratio [42], also avoiding the development of a custom mold. Finally, the material deposition can be limited to the SV to decrease the manufacturing cost further, starting from a preformed central revolved part.

Referring to the last case, a process planning for 8-axis RBAM was adopted [24]. In particular, the authors implemented a 6-axis manipulator, a 2-axis working table, and a laser-based direct metal deposition AM. The framework was specifically developed to manufacture revolved parts. After importing the CAD model, the geometry is firstly decomposed into the core volume and overhanging structures using the algorithm presented in reference [43]. The central hub of the part is realized with a standard planar uniform slicing approach. Then, as depicted in Fig. 2a, the algorithm foresees the intersection of the identified overhangs with a series of offsets of the revolved part surface to obtain the non-planar slicing curves. The adopted offset distance is equal to the desired layer thickness. The obtained slicing curves

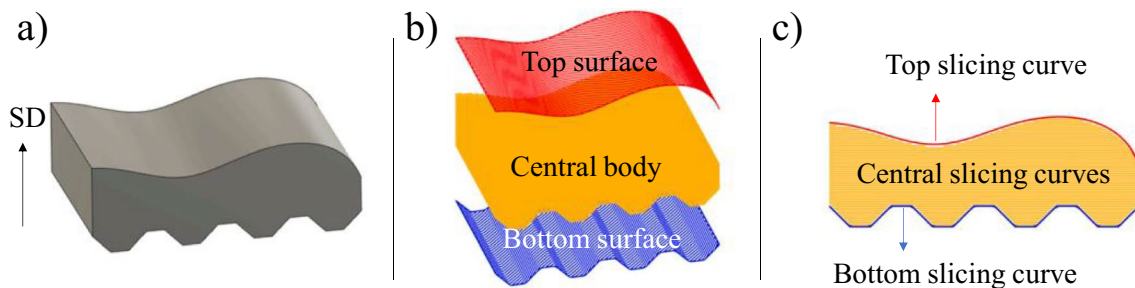
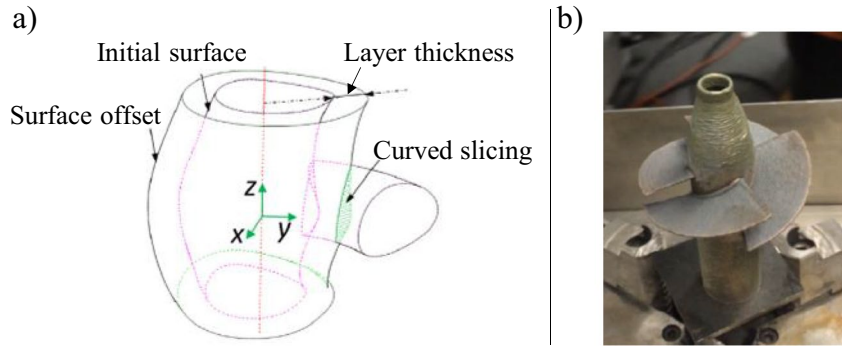


**Fig. 1** Classification of the boundary surfaces of a volume realized by AM: **a** input geometry where SD is the slicing direction; **b** identification of top and bottom surfaces; **c** non-planar slicing applied to the top and bottom surfaces as proposed in reference [32]

**Fig. 2** Revolved slicing process from [24]: **a** main geometrical entities involved in the slicing process; **b** example of a prototypal part being manufactured. In this case, the central cylindrical surface is offset, originating a uniform cylindrical slicing



are divided into small segments to generate the tool path. Also, suitable inverse kinematics have been computed to synchronize the robot arm and the working table. The final produced part is shown in Fig. 2b. This approach was also applied in the work proposed by Ding et al. [44], where a propeller blade is sliced with a constant offset of the central cylindrical surface.

Similarly, the algorithm presented by Zhao et al. [22] includes the intersection of a sequence of surface offset with the geometries of the SVs after a volume decomposition phase (Fig. 3a). In this case, a concave-loop extraction algorithm [29] separates the central cylindrical or conical portion and the connected SVs. Also, this work presents an algorithm that extracts the reference cylinder surface of the input geometry. Then, the layer is processed in its parameter space, recurring to a planar flattening. This way, planar infill processing is applied, and the result is reversely transformed into non-planar slicing curves (Fig. 3b).

Zhao and Guo proposed a similar approach [34], where a framework is developed, suggesting that slicing strategies are selected according to the CAD model features. In this context, cylindrical or conical slicing is set for SVs connected to a cylindrical or conical shape.

Also, variants of the algorithm based on the intersection between a series of cylindrical surfaces and SVs were implemented in few works [45–48]. These algorithms include the infill computation step of the cylindrical curves. Finally, the works developed in references [23, 49] present further algorithms for central cylindrical and conical surfaces. Again, they include analyses and implementation of infill strategies.

To conclude, Table 1 summarizes the main features of the analyzed algorithms from the literature. As noted, the reviewed methods for cylindrical slicing include infill strategies and are sometimes extended to conical geometries. However, non-uniform slicing has yet to be explored in any revised approaches. Thus, the main objective of this paper is to address such a case of non-uniform cylindrical slicing.

### 3 An approach for robot-based, non-uniform cylindrical slicing

This research presents a novel algorithm to process SVs connected to a central cylindrical body for RBAM technology. An original slicing algorithm has been devised and evaluated

**Fig. 3** Non-planar slicing process from [22]: **a** steps of the approach: volume decomposition (left), reference surface offset (right); **b** mapping of the cylindrical surface to a planar one

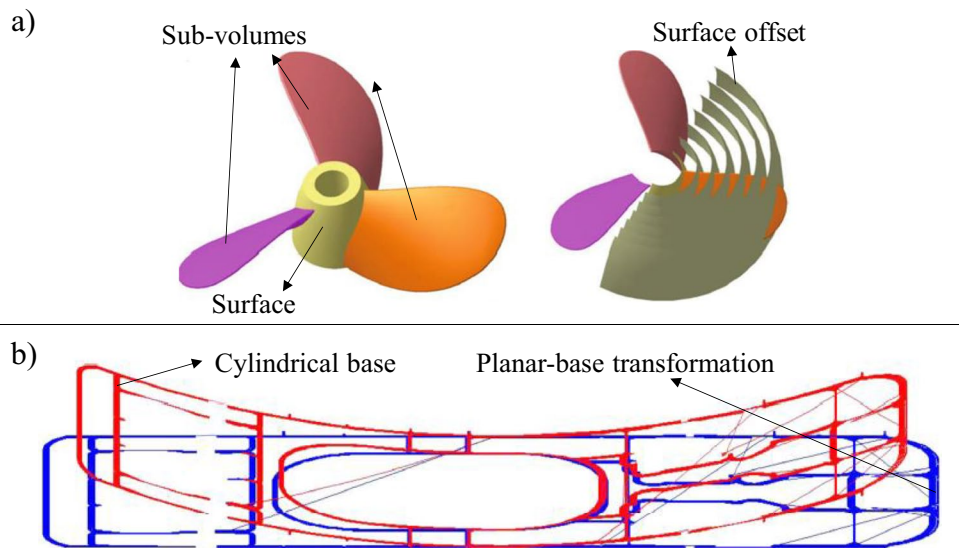


**Table 1** Main characteristics of the reviewed non-planar cylindrical and conical slicing algorithms

Algorithm	Cylindrical slicing	Conical slicing	Infill processing	Non-uniform slicing
Ding Y. et al. [24, 44]	Yes	Yes	Yes	No
Zhao G. et al. [22]	Yes	Yes	Yes	No
He T. et al. [47]	Yes	No	Yes	No
Dharmawan A. G. et al. [48]	Yes	No	Yes	No
Dai F. et al. [23, 49]	Yes	Yes	Yes	No
Wang R. et al. [46]	Yes	No	Yes	No
Yigit et al. [45]	Yes	No	Yes	No

using a reference development framework. The main goal of the framework is to define the procedure for correct and efficient geometry processing in the context of RBAM. In particular, a cylindrical and non-uniform slicing approach is presented, evaluated in terms of expected surface quality, and simulated in a software system for robotic applications to assess the feasibility of the deposition process.

### 3.1 Adopted research framework

Figure 4 shows the main steps of the research workflow, which can be generalized as the design process of any RBAM with a particular focus on non-uniform slicing.

As the first step, the manufacturing set-up must be defined. At this stage, the experimental apparatus is selected, such as the type of AM technology and deposition system (i.e., material extrusion or directed energy deposition). Also, the DoFs of the kinematic system are defined. Generally, a Cartesian 3D printer has 3 DoFs, while robotic cells can be designed with 6 or 8 DoFs [11], adding positioning tables and increasing manufacturing flexibility. Special attention must be given to the gravitational effect on the deposition of the material, which restricts the material pouring directions, thus requiring more DoFs.

In the second step, the process parameters that can be controlled must be selected. Some parameters of the employed deposition process may be controllable by the user, while others are fixed. Controllable variables must be identified and studied to control the quantity of the material being deposited. In particular, experimental campaigns are foreseen to link the controlled process parameters to the bead dimensions [50]. Besides, the geometry processing to elaborate deposition paths strictly depends on such

parameters. Indeed, the available ranges of variability for the layer height and width are defined. The process parameters must continuously change during the material deposition to implement non-uniform path planning strategies.

In the third step, the deposition paths are computed according to a particular strategy: the non-uniform cylindrical one is presented in this paper. In the fourth step, some criteria to assess the expected quality of the final product are defined. This activity optimizes the deposition strategy to maximize the quality of some target portions of the part or pursue some overall objectives. The deposition curves are then converted into a sequence of robot targets necessary to drive the manufacturing process in the robotic cell. Finally, a simulation stage of the deposition process, including the robotic system, is crucial to check the absence of problems such as robot singularities, thus guaranteeing a feasible and successful process. Also, it is advisable to perform thermal simulations, especially for high-energy rate processes such as the deposition of metals.

Coming to the specificity of this paper, the approach is exemplified through an RBAM manufacturing cell with 8 DoFs (Fig. 20). The adopted deposition equipment is the wire and arc additive manufacturing (WAAM) [51] based on the cold metal transfer (CMT) welding technology [52]. The controlled process parameters identification and characterization are based on previous research [50]. The proposed non-uniform cylindrical strategy is then evaluated with a few criteria: the number of layers, the contact area between the SV and the central cylindrical body, the robot path smoothness, and the quality of the top surface. Finally, the slicing curves are converted into a set of robot targets imported in simulation software (i.e., RoboDK<sup>®</sup>) to assess the feasibility of the paths.

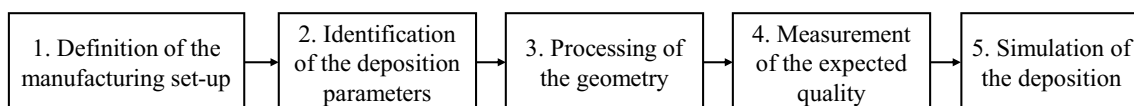


**Fig. 4** The main steps of the adopted workflow that is used to design an RBAM system with non-uniform layer capabilities

### 3.2 Non-uniform cylindrical slicing approach

This section presents a cylindrical slicing approach that takes advantage of non-uniform layer thickness capabilities required by the employed technology. In other words, the deposition means should guarantee the possibility to continuously vary the amount of the added material to realize controllable layer thickness. The scope of processed geometries by this algorithm foresees parts made of a central cylindrical body (*cb*) with connected SVs to be conveniently realized by material deposition. According to the typical B-Rep schema adopted by standard mechanical CAD systems, the input geometry is assumed to be described in analytical solid form. SVs are identified with the concave-loop approach [29].

The idea of the algorithm is based on the following considerations. It is assumed that initial deposited layers must adhere to the substrate shape (i.e., a cylinder). However, the subsequent layers should tend to be planar to facilitate the deposition process. The algorithm described in Fig. 5 demonstrates how non-uniform layer capabilities allow such a transition from cylindrical to planar layers according to the possibilities the adopted technology gives.

In specific terms, three inputs to the algorithm have been selected to describe the working range of the employed technology, i.e., the reference layer height (*hLayer*) and the minimum (*hMin*) and maximum (*hMax*) thickness limits. This means that the generic layer thickness can span between *hMin* and *hMax*, while *hLayer* is identified as the optimal thickness to be adopted as the preferred value. For instance, *hLayer* is selected in the available range, balancing the surface quality and the printing time. In the description of the algorithm, a generic index *i* as a subscript of a variable indicates the *i*th element of an ordered set.

The initial geometry is oriented, so the axis of the cylinder is perpendicular to the *xy* plane. The curve that represents the path of the first layer ( $c_0$ ) is obtained by intersecting the B-Rep of SV (*sv*) with the cylinder lateral surface (*surface*<sub>0</sub>). The curve of the next layer ( $c_1$ ) is obtained by intersecting *sv* with an offset of the cylinder surface, i.e., *surfaces*<sub>1</sub>, at a distance *hLayer*, getting a second cylinder with a larger diameter (Fig. 6a, b).

The curves  $c_0$  and  $c_1$  are projected onto the *xy* plane, thus obtaining two arcs,  $a_0$  and  $a_1$  (Fig. 6b). The ends of the arc  $a_1$  are connected by the segment  $s_1$  (Fig. 7). If this segment does not intersect *surface*<sub>0</sub>, the distance *d* between the midpoint of  $a_0$  (*middleArc*) and the closest point of this midpoint concerning  $s_1$  (*closestPoint*) is calculated, as depicted in Fig. 7a. If *d* is greater than or equal to the minimum layer thickness limit (*hMin*),  $s_1$  is extruded along *Z*+, generating a new *surfaces*<sub>1</sub>. This surface is intersected with *sv*, developing a new flat layer (Fig. 7d). Subsequent layers are obtained by translating this surface along its normal at each iteration

by an amount equal to *hLayer* and intersecting the translated surface with *sv* to complete the slicing.

Instead, if *d* is lower than the minimum limit of the thickness of the layer, a segment *line* is generated between the ends *arcMidPoint* and *closestPoint*. Then, *line* is evaluated according to *hMin*, finding a point  $P_2$  (Fig. 7b). In this way, a circle is constructed, passing through 3 points: the two ends of  $a_1$  ( $P_1$  and  $P_3$ ) and  $P_2$  (Fig. 7c). This circle is extruded along *Z*+ to obtain a new cylindrical surface (*surfaces*<sub>1</sub>). This surface is intersected with *sv*. As a result, a new curve with lower curvature compared to  $a_1$  is obtained. Then, *surfaces*<sub>1</sub> is offset by a quantity equal to the *hLayer*, and the process is repeated until the slicing is completed, moving progressively to planar layers.

Similar to Fig. 7b, if the segment  $s_1$  intersects *surface*<sub>0</sub>, a segment *line* is constructed between *arcMidPoint* and the closest point of *arcMidPoint* concerning  $a_1$  (*closestPoint*) (Fig. 8a). The line length is evaluated using *hMin*, finding a new point  $P_2$  (Fig. 8b). In this way, a new circle is built that passes through 3 points: the two ends of  $a_1$  ( $P_1$  and  $P_3$ ) and  $P_2$  (Fig. 8c). As before, this circle is extruded to obtain a new cylindrical surface (*surfaces*<sub>1</sub>) that is intersected with *sv*, resulting in a new curve  $c_1$ . The process is repeated until slicing is complete.

The resulting surfaces are depicted in Fig. 9. In particular, Fig. 9a shows a planar surface created by the extrusions of a segment *s* (Fig. 7d). Figure 9b represents a cylindrical surface obtained through the extrusions of a circle (Fig. 7c and Fig. 8c). Figure 9c depicts all the surfaces built to slice the SV.

The script and all the abovementioned steps are formalized in the pseudo-code presented in the 0 The algorithm was developed using Rhinoceros 3D<sup>®</sup> and the Grasshopper<sup>®</sup> package for visual programming. Grasshopper<sup>®</sup> provides many functionalities that mostly overlap with the interactive commands in Rhinoceros 3D<sup>®</sup>. Such functionalities are available as blocks that can be inserted in a graphic board and connected with virtual wires representing values and geometrical entities exchange.

Python or C# blocks can be defined, containing custom-made code for more advanced functionalities. In particular, the block *Non-planar slicing* contains the Python scripts described in Algorithms 1 and 2. The functions listed in the pseudo-code have been implemented directly, recalling or combining native functions. The inputs of the block are the layer height (*hLayer*), the maximum layer thickness (*hMax*), the minimum layer thickness (*hMin*), the SV B-Rep (*sv*), and the surface of the central body (*cb*). The block outputs are a set of slicing curves (*c*) and the slicing surfaces (*surfaces*) graphed in a Rhinoceros 3D<sup>®</sup> environment.

A typical output of the application of the algorithm can be seen in Fig. 10. The figure shows the Python block in Grasshopper<sup>®</sup> that implements the pseudo-code presented in the 0 In the Rhinoceros 3D<sup>®</sup> environment, the trend of the slicing surfaces can be appreciated for a propeller model (Fig. 11).

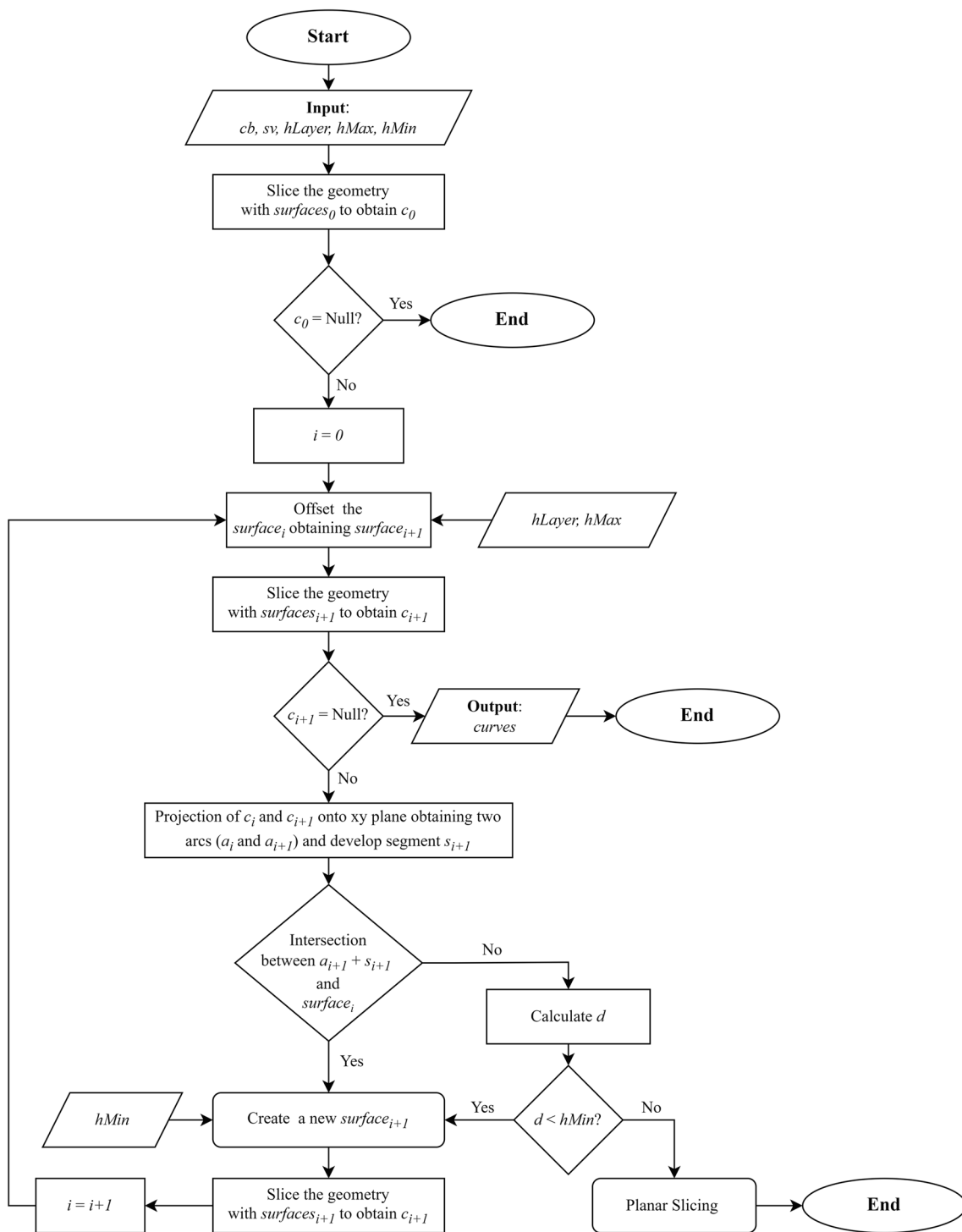


**Fig. 5** The overall workflow of the non-uniform cylindrical slicing algorithm. *cb*, surface of the central cylindrical body; *sv*, Brep of the SV; *hLayer*, layer height; *hMax*, maximum manufacturable thickness;

*hMin*, minimum manufacturable thickness; *c<sub>i</sub>*, *i*th curve; *surface<sub>i</sub>*, *i*th surface; *a<sub>i</sub>*, *i*th arc; *s<sub>i+1</sub>*, *i* + 1th segment; *d*, distance between the midpoint of *a<sub>i</sub>* and the closest point of this midpoint concerning *s<sub>i+1</sub>*

#### 4 Evaluation of the proposed algorithm

The proposed algorithm has been evaluated compared to two alternative slicing strategies that are consolidated

approaches as emerged from the literature, i.e., multi-directional planar uniform slicing [29] and uniform cylindrical slicing [24, 45, 46]. Four assessing criteria have been used to evaluate the expected results for each model and slicing

**Fig. 6** Non-planar cylindrical slicing algorithm: **a** input geometry, identification of the central body and the SVs, an offset of the cylindrical surface; **b** curves  $c_0$  and  $c_1$  resulting from the first iteration and their projection  $a_0$  and  $a_1$  to the  $xy$  plane

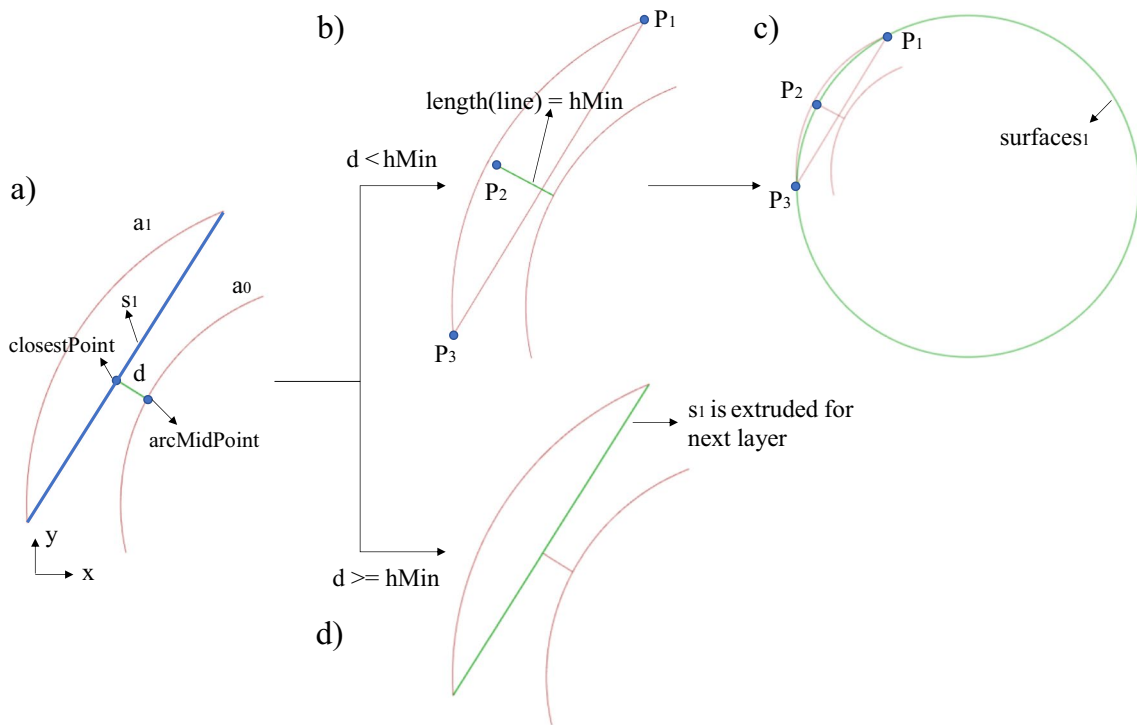
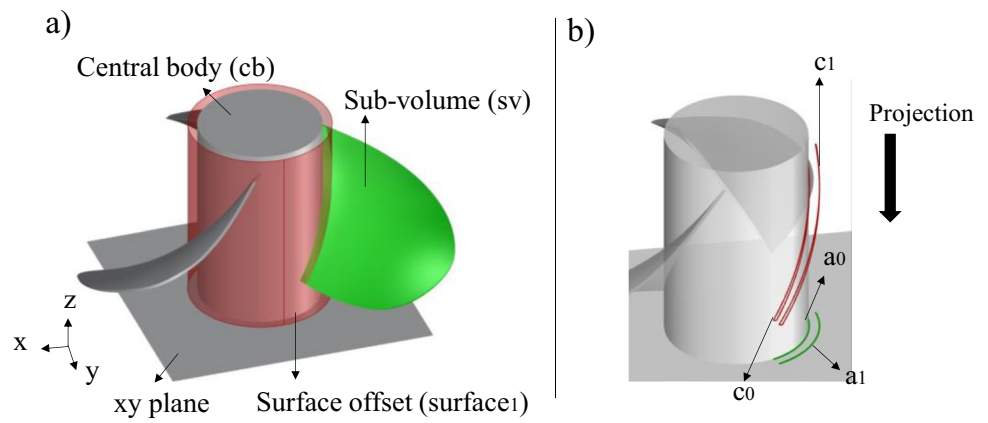


**Fig. 7** Procedure for the construction of the curve which represents the trace on the  $xy$  plane of the surface of the next layer, case 1: **a** construction of  $s_1$ , evaluation of the distance  $d$  for the case it is lower

than  $hMin$ ; **b** construction of  $P_2$  along  $line$ ; **c** construction of a circle that passes through  $P_1$ ,  $P_2$ , and  $P_3$ ; **d** the segment  $s_1$  is used to obtain the planar  $surfaces_1$

algorithm combination. In particular, the following indicators have been adopted:

- The *number of slicing surfaces* ( $NL$ , Fig. 12a). Reducing the number of layers generally leads to lower manufacturing time and fewer defoliation problems.
- The *adhesion area* ( $A$ ) [ $mm^2$ ] is at the interface between the SV and the central body. This indicator provides information about the quality of the bottom layer. A large contact area generally corresponds to an improved connection between the central body and the SV. According to the

slicing approach, one or more layers can realize the link at the interface. To estimate the contribution of each layer, only the portions of the slicing curves included within 50% of the layer height have been considered, as depicted in Fig. 12b. This value was selected as an approximation of the actual adhesion region. Such an index coincides with the bottom surface only when the first layer is realized as an offset of the cylindrical bottom surface.

- The *number of robot targets* in the paths generated from the slicing curves ( $NV$ ). According to the workflow depicted in Fig. 4, the slicing curves are transformed



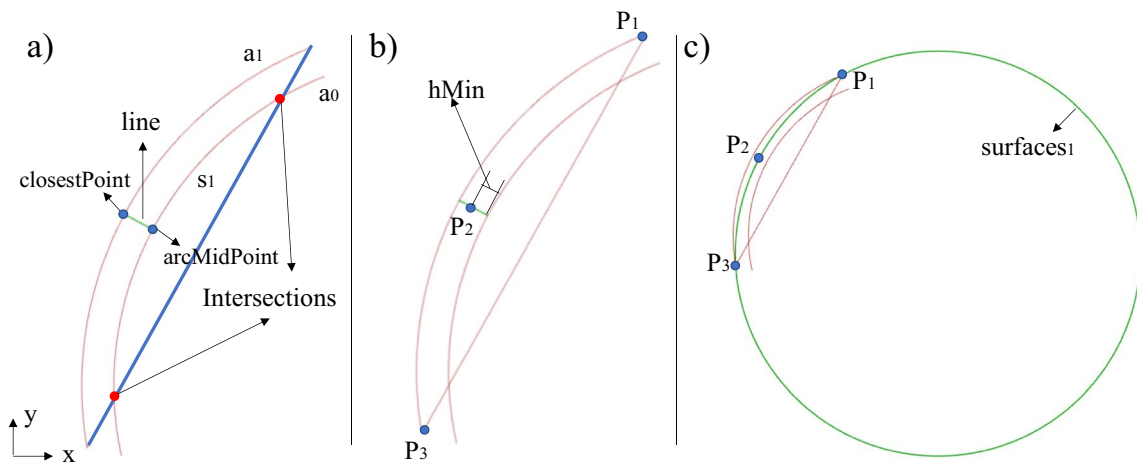


**Fig. 8** Procedure for the construction of the curve which represents the trace on the  $xy$  plane of the surface of the next layer, case 2: **a** construction of  $s_1$ ,  $arcMidPoint$  and  $line$ ; **b** construction of  $P_2$  along  $line$ ; **c** construction of a circle that passes through  $P_1$ ,  $P_2$ , and  $P_3$

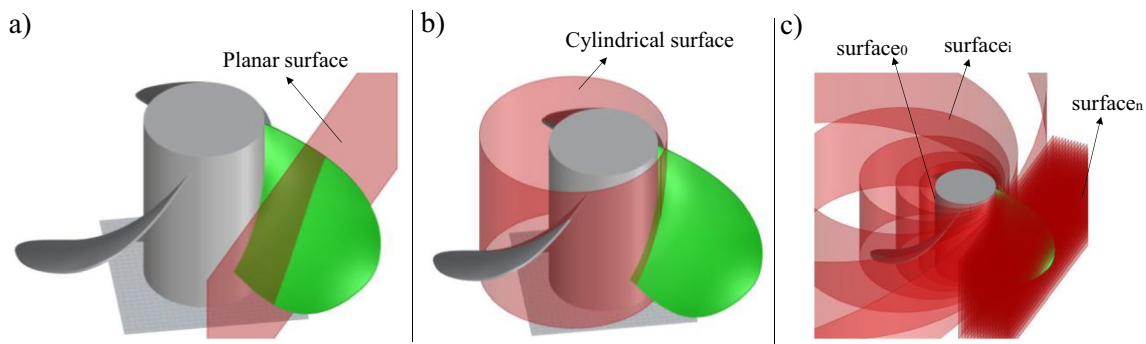


**Fig. 9** Resulting layer surfaces from the process iteration: **a** first planar surface; **b** cylindrical surface at step 1; **c** complete sequence of surfaces, i.e.,  $surface_0$ , the first surface of slicing;  $surface_i$ , the  $i$ th surface of slicing;  $surface_n$ , last slicing surface

into polylines (Fig. 12c) depending on a sampling strategy that ensures two conditions: a maximum deviation tolerance between the curve and the polyline and a minimum length of each segment. Once such parameters have been fixed according to the accuracy and motion possibilities of the adopted robotic system, a lower NV parameter indicates better suitability of the paths to be followed by the robotic system since fewer changes of robot poses are present. As a rule of thumb, planar layers reduce the required robot targets. In the test cases reported in the following sections, the maximum deviation tolerance has been assumed to be equal to 0.3 mm, while the minimum edge length is equal to 3 mm.

- The *average angles* [rad] formed by the deposition directions along the final slicing curve and the normal to the top surface ( $R$ ). High values of this angle mean that the error between the deposited material level and the surface model is high because of the steps created by the discrete layer height (Fig. 12d). Such an error

is also known as cusp height and is primarily relevant, especially on the top surface.

The four numerical indices have been used to compare the performances of the three considered algorithms on four test geometries (Fig. 13). The first test case is a propeller whose bounding box measures  $82.6 \times 80.7 \times 43.2$  mm (Fig. 13a). One blade is taken into consideration as the processed SV. The second case study is depicted in Fig. 13b. It is a support taken from [29], whose bounding box measures equal to  $60 \times 111 \times 110$  mm. In this case, three SVs are processed with the considered slicing algorithms. A scaled boiler (Fig. 13c) model with a bounding box measure equal to  $100 \times 157 \times 200$  mm is processed as a third test case where two SVs are considered. Finally, a simplified valve body with a bounding box measures  $290 \times 230 \times 200$  mm is elaborated as the fourth test case (Fig. 13d). In the experimentation, the realization of the

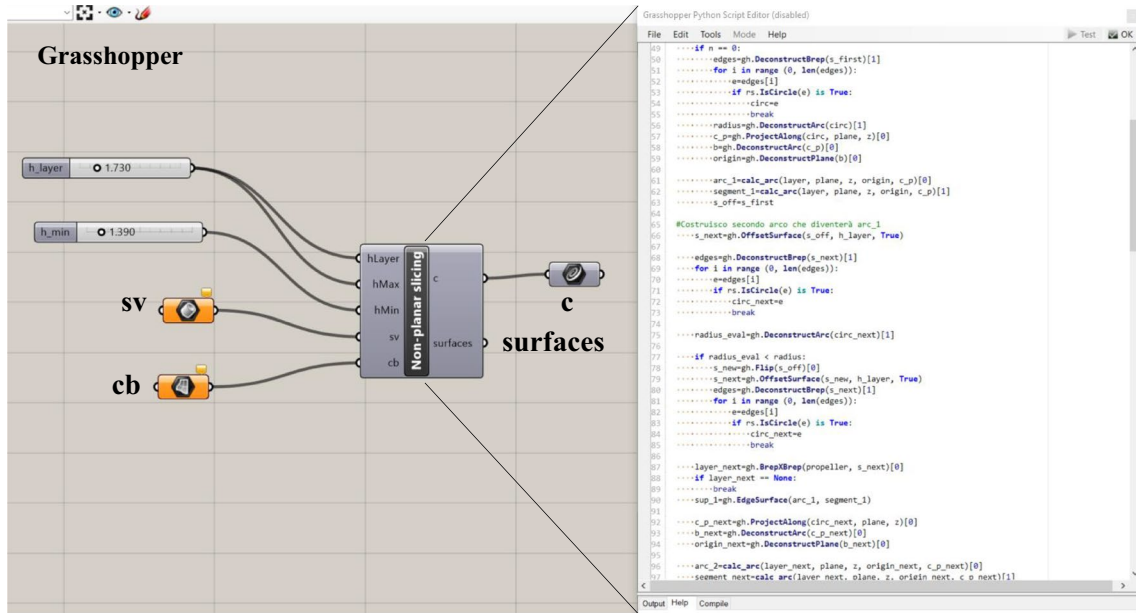


Fig. 10 Implementation in Grasshopper® of the non-uniform cylindrical slicing algorithm as a Python script block

central cylindrical body is neglected, while each SV is sliced according to the three different slicing strategies.

To process the geometries according to realistic slicing parameters, an interval of reference values to vary the

layer height was derived from an experimental campaign. A CMT-based WAAM was selected as deposition technology, and the obtained results are reported in [50]. For the present study, the reference slicing height is chosen equal to 1.73 mm ( $h_{Layer}$ ), with a minimum value no lower than 1.39 mm ( $h_{Min}$ ). Such values were used to compute the slicing for the four test cases.

The indices were calculated by adding a processing step in the Rhinoceros 3D® environment, again using the Grasshopper® programming tool. The obtained results are reported as follows.

Figure 14 depicts the slicing curves obtained for the case study shown in Fig. 13a. Table 2 summarizes the numerical indices computed for the three slicing algorithms.

Figure 15 and Fig. 16, respectively, depict the slicing curves for the test cases shown in Fig. 13b, c. Table 3 and Table 4 summarize the indices of the three slicing algorithms.

Finally, the slicing results of the last example (Fig. 13d) are shown in Fig. 17. The obtained indices are reported in Table 5.

### 5 Analysis of the results

This section shows the main results of the three algorithms according to the criteria summarized in the previous tables. Then, the slicing curves of the propeller test case (Fig. 13a) are imported into RoboDK® to test the feasibility of the robot paths.

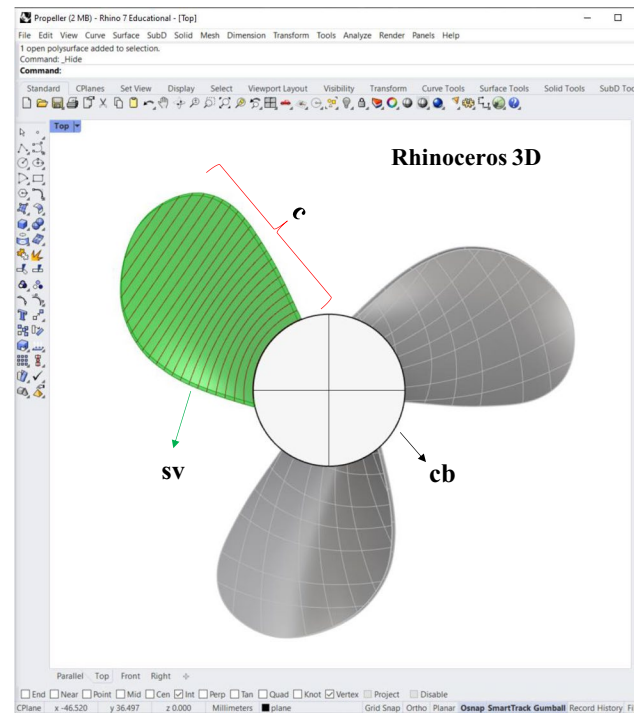
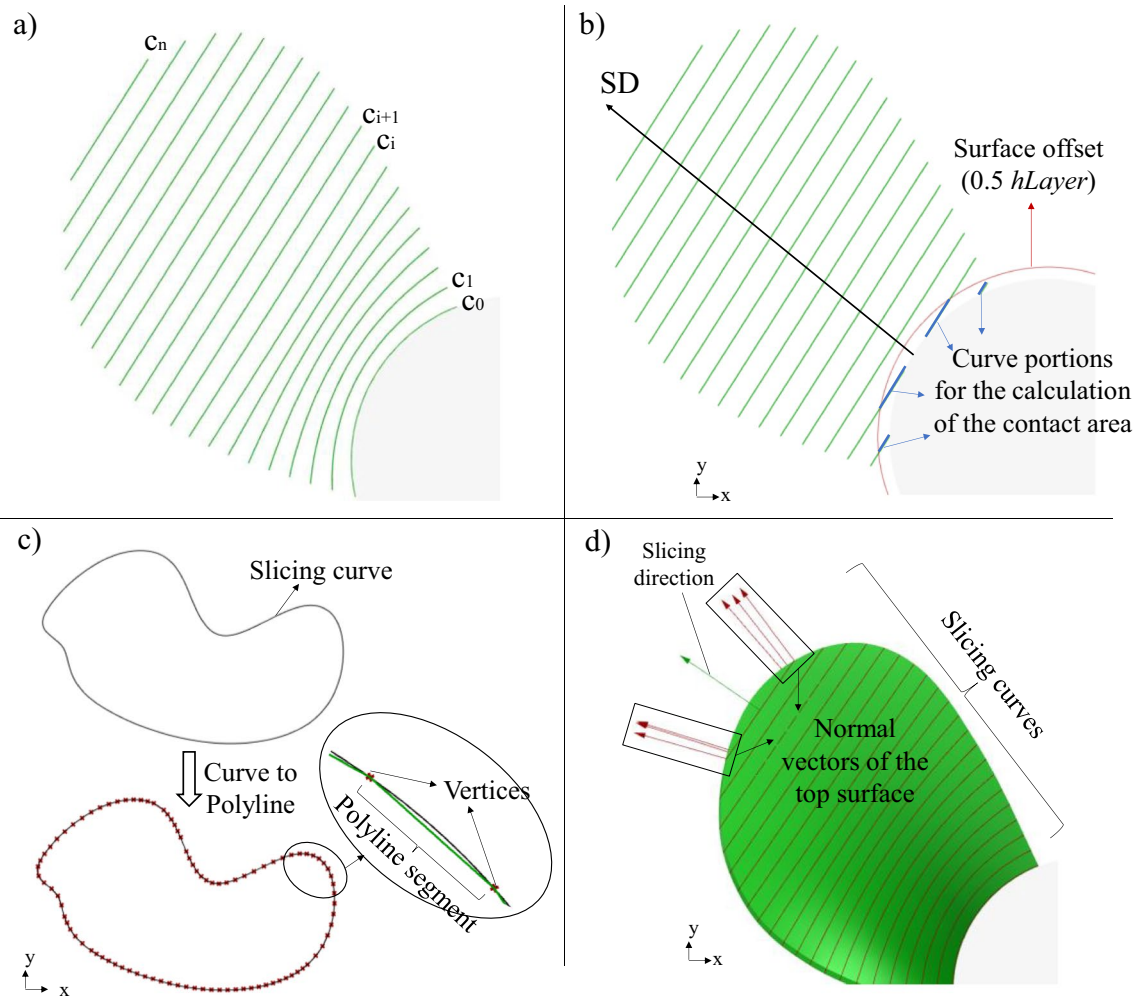


Fig. 11 Visualization in Rhinoceros 3D® environment of the obtained sequence of layers



**Fig. 12** Illustration of the indices adopted to evaluate the proposed slicing approach. **a** Number of slicing curves; **b** estimation of the contact area; **c** conversion of a slicing curve into a polyline, i.e., a

sequence of segments connecting robot targets; **d** normal vectors to calculate the *R* index

### 5.1 Discussions of the numerical indices

This section compares the three algorithms based on the results reported in the previous tables. In particular, the computed indices have been normalized from 0 to 1, with 1 representing the optimal condition. The following equations have been used for this aim.

$$I_1 = 1 - \frac{NL_i}{\sum_{i=1}^3 NL_i} \tag{1}$$

$$I_2 = \frac{A_i}{\sum_{i=1}^3 A_i} \tag{2}$$

$$I_3 = 1 - \frac{NV_i}{\sum_{i=1}^3 NV_i} \tag{3}$$

$$I_4 = 1 - \frac{R_i}{\sum_{i=1}^3 R_i} \tag{4}$$

The subscript *i* identifies one of the three investigated algorithms. A total reached score (*F*) has also been calculated by adding the contribution of each criterion, as in Eq. 5.

$$F = I_1 + I_2 + I_3 + I_4 \tag{5}$$

Table 6 summarizes the scores resulting from the propeller test case (Fig. 13a). The uniform cylindrical slicing obtains the highest score. Indeed, it presents the same

**Fig. 13** Test cases for the algorithm evaluation: **a** propeller; **b** support (taken from [29]); **c** scaled boiler model; **d** simplified valve body

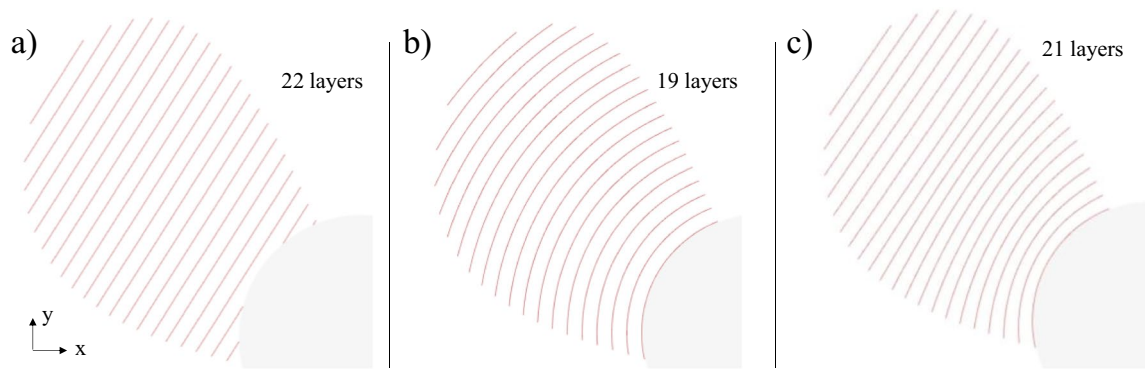
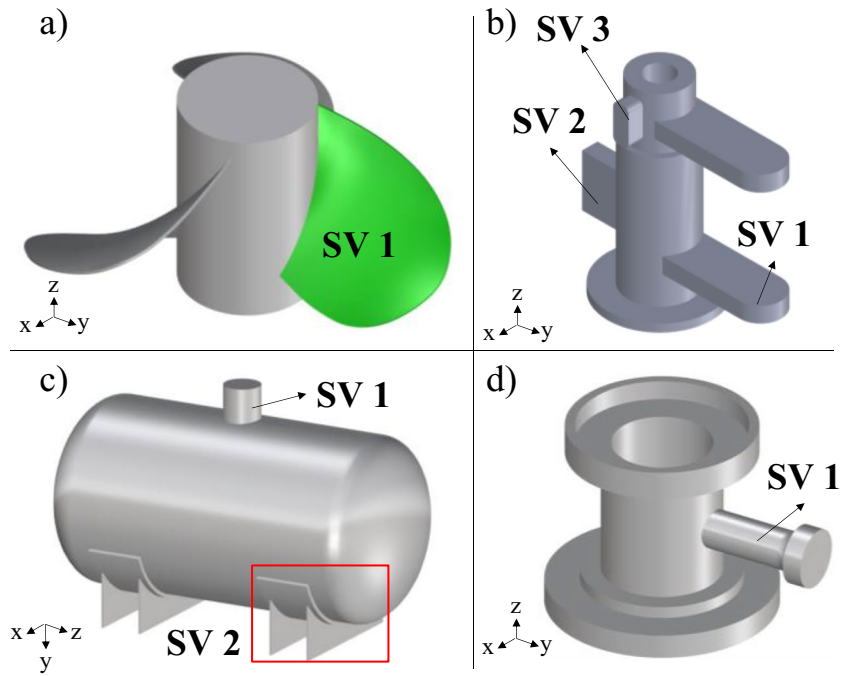


**Fig. 14** Slicing results for the propeller test case adopting: **a** multi-axial planar uniform slicing; **b** cylindrical slicing; **c** proposed non-uniform cylindrical slicing

contact area ( $I_2$ ) as the proposed approach while increasing the top surface’s accuracy ( $I_4$ ). However, the proposed approach reduces the total number of robot targets to uniform cylindrical slicing ( $I_3$ ).

Table 7 shows the scores of the three algorithms related to the three SVs of the support case study (Fig. 13b). The proposed slicing algorithm has the best final scores for

**Table 2** Slicing results for the propeller test case

Criterion	Planar uniform slicing	Cylindrical slicing	Proposed algorithm
NL	22	19	21
A [mm <sup>2</sup> ]	8.09	25.37	25.37
NV	211	269	242
R [rad]	0.38	0.30	0.42

each SV. It is particularly suited for the SV2 and SV3 as the top surface is well approximated ( $I_4$ ), and the contact area is high ( $I_2$ ). As can be noted from Table 7, the cylindrical slicing is performing not so well for SV2 and SV3. Indeed, the top surface is poorly approximated ( $I_4$ ), and the number of vertices is high ( $I_3$ ).

Table 8 summarizes the final scores of the two SVs of the scaled boiler (Fig. 13c). The proposed algorithm is the best slicing approach for SV1 and SV2, presenting the highest  $F$  index for both SVs. Indeed, it offers the same contact area of the uniform cylindrical slicing ( $I_2$ ) while it optimizes the top surface ( $I_4$ ). Also, it reduces the number of vertices compared to uniform cylindrical slicing ( $I_3$ ).

Table 9 describes the scores of the three algorithms applied to the valve test case (Fig. 13d). Also, in this case study, the proposed approach outperforms the others.

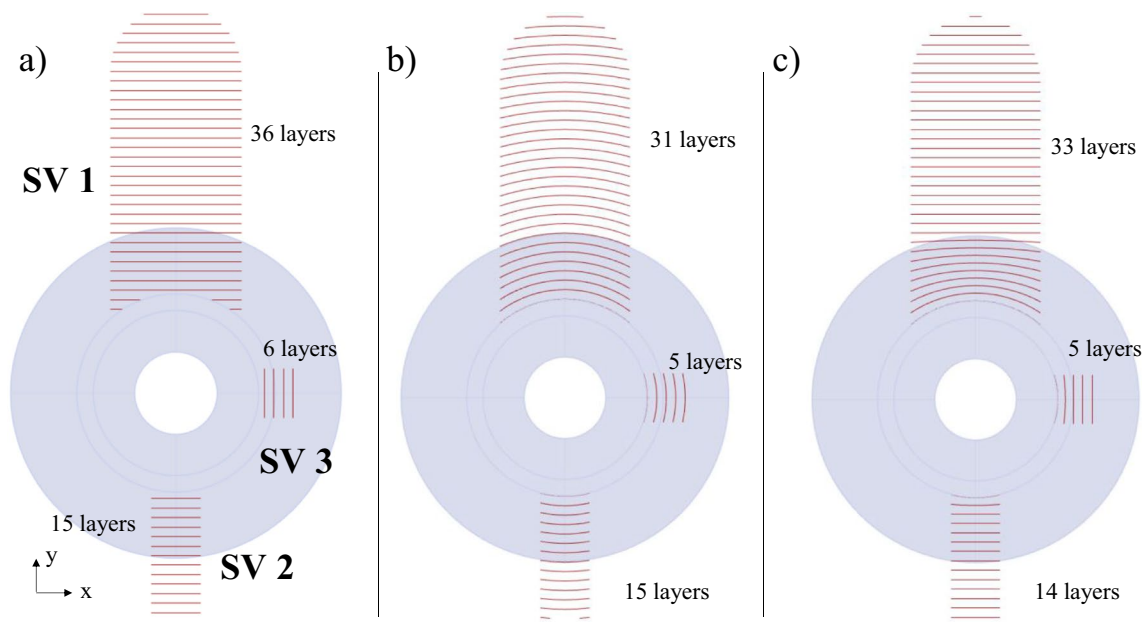


Fig. 15 Slicing results of the support test case: **a** multi-axial planar uniform slicing; **b** cylindrical slicing; **c** proposed algorithm

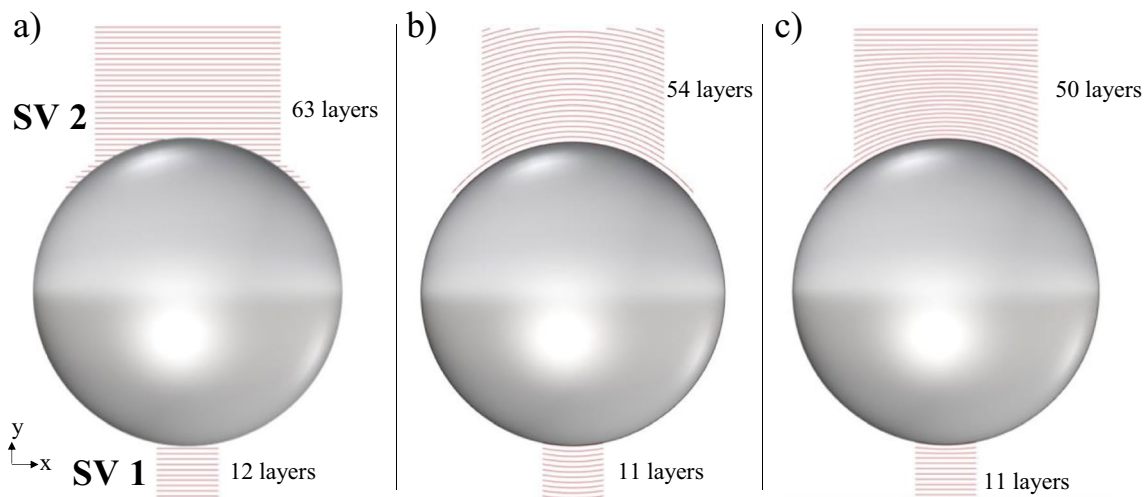


Fig. 16 Slicing results of the scaled boiler: **a** multi-axial planar uniform slicing; **b** cylindrical slicing; **c** proposed algorithm

Table 3 Slicing results of the support case study

Criterion	Planar uniform slicing			Cylindrical slicing			Proposed algorithm		
	SV1	SV2	SV3	SV1	SV2	SV3	SV1	SV2	SV3
NL	36	15	6	31	15	5	33	14	5
A [mm <sup>2</sup> ]	132.0	60	30	233.88	272.86	247.45	233.88	272.86	247.45
NV	176	71	50	399	115	55	247	76	55
R [rad]	0.52	0	0	0.24	0.09	0.15	0.10	0	0

Indeed, it combines the benefits of cylindrical slicing (high value of  $I_2$ ) and planar slicing (high value of  $I_4$ ). Also, the number of vertices generated by the proposed approach is similar to that of the planar slicing ( $I_3$ ).

As a final remark, it is essential to note that the application of the sectioning process may lead to some portions of the curves whose distance from the substrate is below the imposed  $hMin$ . This problem is highlighted in Fig. 18 for

**Table 4** Slicing results of the scaled boiler test case

Criterion	Planar uniform slicing		Cylindrical slicing		Proposed algorithm	
	SV1	SV2	SV1	SV2	SV1	SV2
NL	12	63	11	54	11	50
A [mm <sup>2</sup> ]	8.70	115.17	315.76	2623.23	315.76	2623.23
NV	226	391	242	1134	242	830
R [rad]	0	0	0.1	0.32	0	0

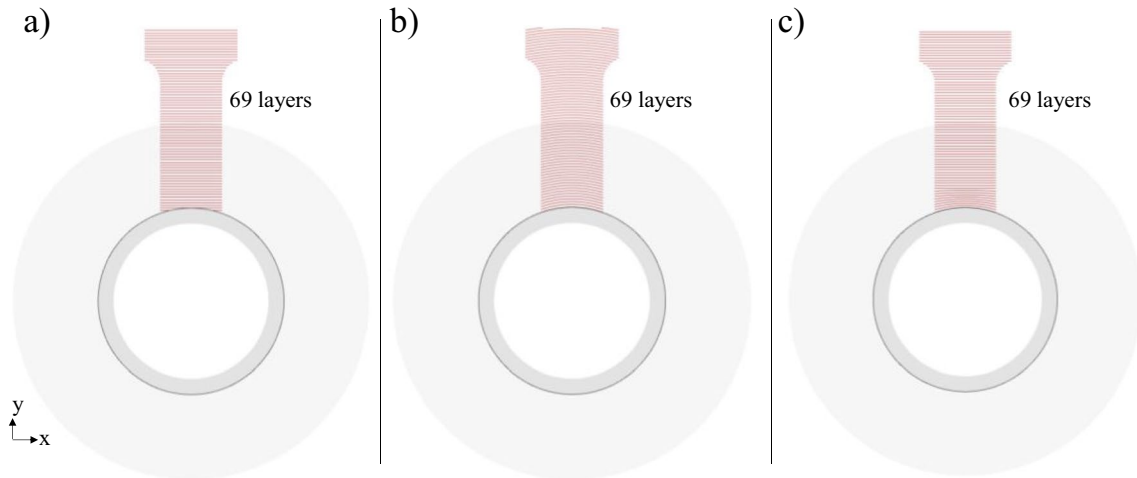


**Fig. 17** Slicing results of the simplified valve body: **a** multi-axial planar uniform slicing; **b** cylindrical slicing; **c** proposed algorithm

**Table 5** Slicing results of the valve part case study

Criterion	Planar uniform slicing	Cylindrical slicing	Proposed algorithm
NL	69	69	69
A [mm <sup>2</sup> ]	296.25	1274.80	1274.80
NV	2812	3003	2878
R [rad]	0	0.15	0

**Table 6** Final scores for the propeller test case

Index	Planar uniform slicing	Cylindrical slicing	Proposed algorithm
$I_1$	0.65	0.69	0.66
$I_2$	0.14	0.43	0.43
$I_3$	0.71	0.63	0.67
$I_4$	0.66	0.72	0.62
$F$	<b>2.16</b>	<b>2.47</b>	<b>2.38</b>

the propeller and the boiler test cases. A specific correction to the generated paths is necessary to avoid infeasible deposition regions.

The obtained results depend on the selected limits for the layer thickness, which vary according to the deposition

means. As shown by the four cases above, the specific shape strongly influences the obtained indices. The proposed evaluation index ( $F$ ) merges different aspects of the geometry, particularly the bottom and top surface characteristics. Therefore, the slicing approach to be preferred depends on the application context. The provided capability of the algorithm to be tuned by the three parameters  $hMax$ ,  $hMin$ , and  $hLayer$  allows the necessary degree of freedom to cope with the specificity of the shape, also reducing the approach to a standard cylindrical slicing if the three numbers are collapsed to the same value.

### 5.2 Robot path computation and simulation

As introduced in Fig. 4, the robot path computation and simulation are crucial steps to assess the feasibility of reaching locations. The conversion of the slicing curve into a series of targets requires, at first, the identification of the positions along the curve itself. Then, a plane is created at each position, representing the target orientation (Fig. 19, left). Indeed, the planes store the robot tool head's position and orientation. Note that the normal vector of each plane is aligned with the normal vector of the slicing surface at the considered point, i.e., the origin of the plane.

The sequence of robot targets is generated for each slicing curve. The computed locations are visualized in the

**Table 7** Final scores for the support case study

Index	Planar uniform slicing			Cylindrical slicing			Proposed algorithm		
	SV1	SV2	SV3	SV1	SV2	SV3	SV1	SV2	SV3
$I_1$	0.64	0.66	0.63	0.69	0.66	0.69	0.67	0.69	0.69
$I_2$	0.22	0.10	0.06	0.39	0.45	0.47	0.39	0.45	0.47
$I_3$	0.79	0.73	0.69	0.52	0.56	0.66	0.70	0.71	0.66
$I_4$	0.39	1	1	0.72	0	0	0.89	1	1
$F$	<b>2.04</b>	<b>2.49</b>	<b>2.38</b>	<b>2.32</b>	<b>1.67</b>	<b>1.82</b>	<b>2.65</b>	<b>2.85</b>	<b>2.82</b>

**Table 8** Final scores of the boiler case study

Index	Planar uniform slicing		Cylindrical slicing		Proposed algorithm	
	SV1	SV2	SV1	SV2	SV1	SV2
$I_1$	0.65	0.62	0.68	0.68	0.68	0.70
$I_2$	0.01	0.18	0.49	0.41	0.49	0.41
$I_3$	0.68	0.83	0.66	0.52	0.66	0.65
$I_4$	1	1	0	0	1	1
$F$	<b>2.34</b>	<b>2.63</b>	<b>1.83</b>	<b>1.61</b>	<b>2.83</b>	<b>2.76</b>

**Table 9** Final scores of the valve case study

Index	Planar uniform slicing	Cylindrical slicing	Proposed algorithm
$I_1$	0.67	0.67	0.67
$I_2$	0.10	0.45	0.45
$I_3$	0.68	0.65	0.67
$I_4$	1	0	1
$F$	<b>2.45</b>	<b>1.77</b>	<b>2.79</b>

Rhinoceros 3D<sup>®</sup> environment and exported in a text file that contains the robot target origin and orientation of the deposition means (Fig. 19). This file is then imported into the robot simulation environment. In this research, the RoboDK<sup>®</sup> system has been employed, given its capability

to simulate the robot paths, evaluating the reachability of each target location according to the provided robot kinematic. In particular, Fig. 20 depicts the 8 DoF robot cells used for the simulation.

A working table with 2 DoFs (KUKA KP2-HV500) and a robot with 6 DoFs (KUKA KR 70 R2100) are implemented. The imported path and the propeller geometry are referred to the center of the working table. The propeller is positioned on the top of a support to simulate a real manufacturing scenario. A CMT welding torch is used as a deposition tool.

In metallic RBAM, gravity can strongly affect the output quality, hindering the realization of the part or reducing the surface finish [53]. In this context, a working table can align the material deposition direction with the direction of gravity, allowing the stability of the deposition. So,

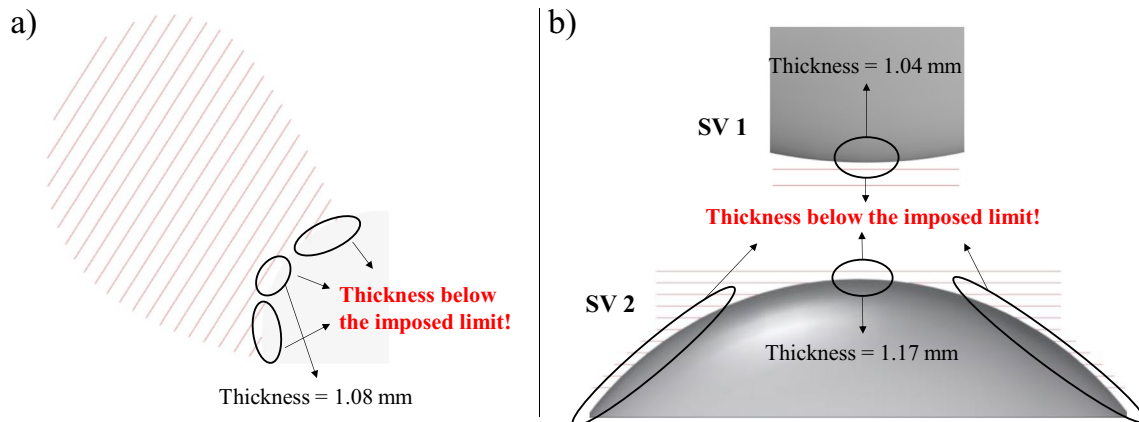


**Fig. 18** Problem with the multiaxial uniform planar slicing: **a** propeller test case; **b** boiler test case

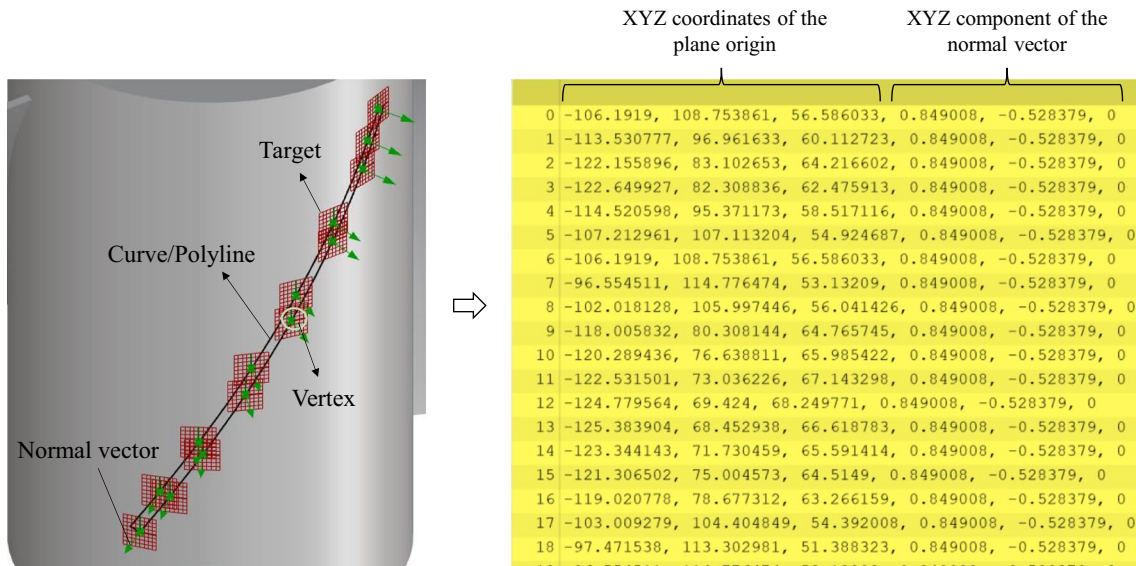


Fig. 19 Representation of the robot targets in the Rhinoceros 3D® graphical environment and export file to RoboDK®

an initial rotation of the first external axis equal to  $-45^\circ$  has been tested to reduce the effect of gravity, as in Fig. 21. However, this choice was not feasible since the manipulator could not reach all the targets of the input file due to singularities in the robotic arm configurations.

Next, the rotations of the table were changed to avoid singularities and collisions. In particular, the first external table axis rotation was imposed to  $90^\circ$  while the second rotation was set to  $180^\circ$ . These rotations are maintained fixed during the simulation. As can be noted from Fig. 22, the robot path is solved without singularities and collisions.

### 6 Conclusions

Non-planar and non-uniform slicing can increase the adhesion among surface finish layers, reduce the need for support structures, and allow efficient manufacturing of low-quantity batches of customized parts characterized by low fly-to-buy ratios. The manufacturing architecture based on anthropomorphic robots is a powerful enabler to implement such advanced deposition strategies, which overcomes traditional limits of the consolidated 3D printers. In this context, advanced slicing algorithms are needed to utilize such extended technological capabilities.

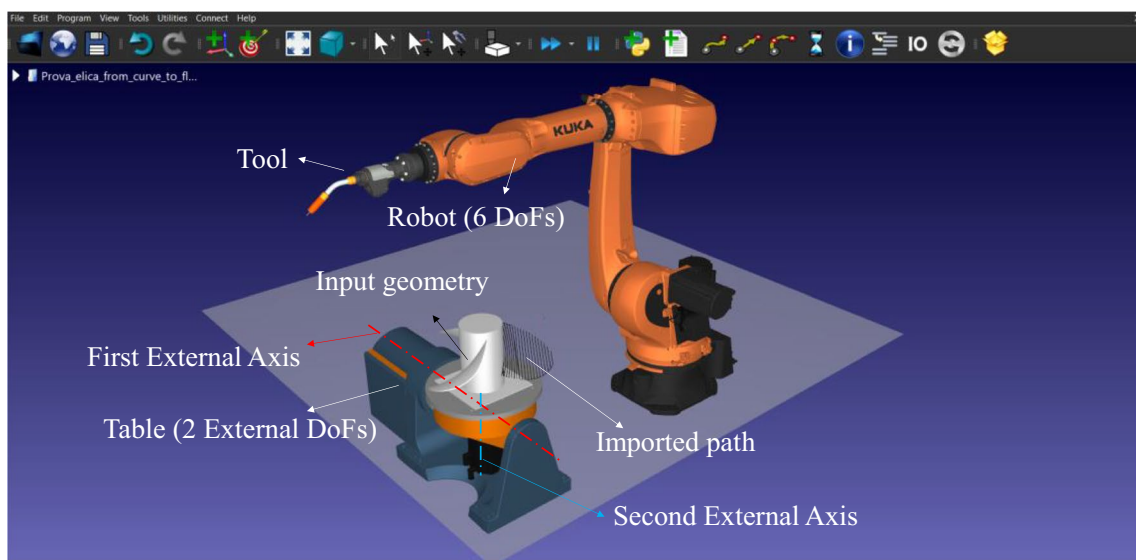


Fig. 20 Robot cell with 8 DoFs in RoboDK®. All the mechanisms are represented in their home position



Contrary to the reviewed approaches, this paper has focused on a non-uniform cylindrical slicing algorithm that modulates the layer's shape from cylindrical to planar according to set limits on the layer thickness. The algorithm was applied to four geometries and compared with the other two existing slicing strategies. The results highlighted that the algorithm guarantees a better adhesion between the central body and the SVs in the first layers compared to the multiaxial planar slicing. Also, it considers and simplifies the path approximation of the robot. Indeed, planar curves usually present fewer path discontinuities compared to non-planar paths. This corresponds

to a reduction of tool head rotations and direction changes in comparison to the uniform cylindrical slicing. Also, the algorithm is highly suited for SVs that present a planar top surface, increasing the approximation of this feature compared to the uniform cylindrical slicing. A software architecture composed of Rhinoceros 3D®, Grasshopper®, and RoboDK® has been developed. It implements the proposed slicing strategy and validation using a general framework to devise and assess RBAM approaches for slicing algorithms.

Although the results of the proposed algorithm are promising, the work has some limitations. In fact, the

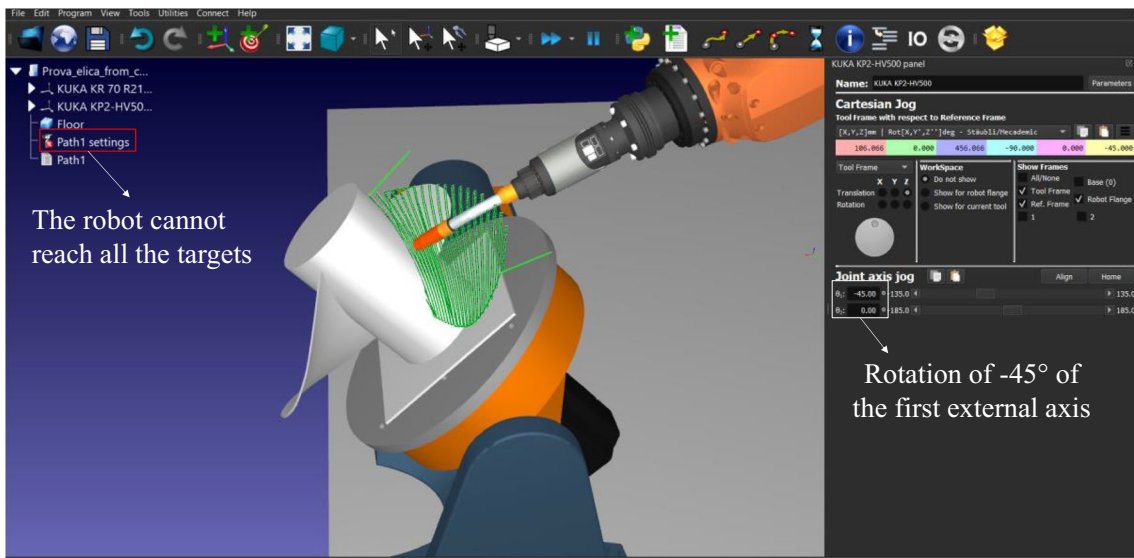


Fig. 21 Reachability and singularities problems in the robot paths

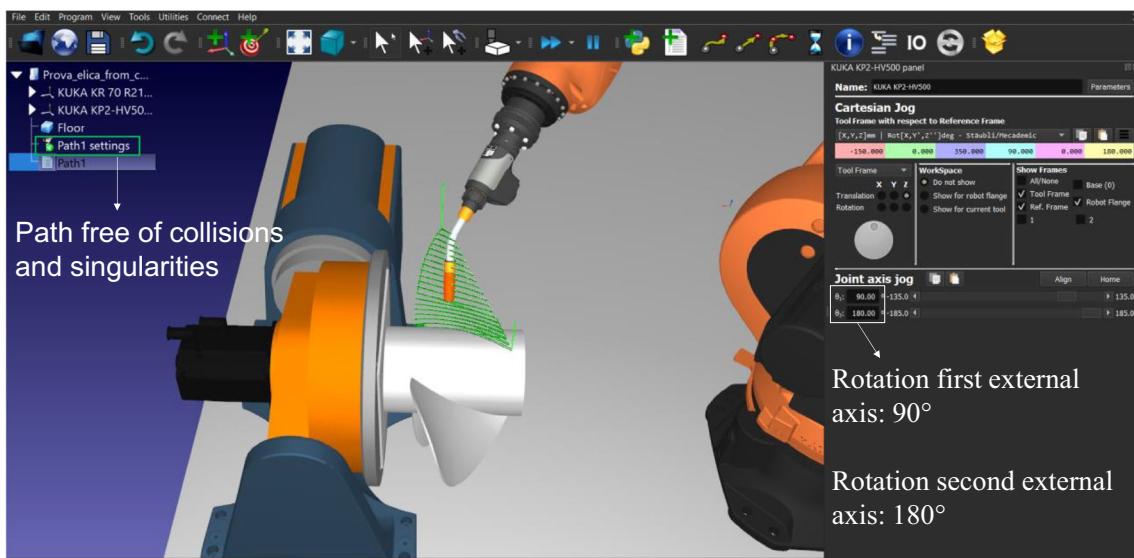


Fig. 22 Robot path free of collisions and singularities

algorithm can be applied only to cylindrical bodies. Furthermore, the validation has been performed on a virtual basis. The manufacturing of parts with real robots and welding torches can highlight other issues that were not recognized through simulation.

Therefore, as future directions, the proposed algorithm can be extended to generic revolved bodies, also implementing an infill strategy. Then, the non-uniform slicing should be adapted to more complex part shapes, dynamically adapting the layer shape according to the boundary surface of the part to optimize the overall surface finish.

Manufacturing test cases is a further step to confirm the results reached so far in virtual environments and confirm the feasibility of the proposed approach. Finally, given the higher complexity of the robotic system compared to standard Cartesian solutions, implementing costs must also be carefully assessed and balanced with the increased quality of the realized parts. In particular, costs can be strongly reduced by implementing specific product configuration solutions [54] to support the design phase, taking advantage of the flexibility of RBAM solutions for the realization of customized products.

## Appendix. Pseudo-code of non-uniform cylindrical slicing

ALGORITHM 1: NON-UNIFORM CYLINDRICAL SLICING ALGORITHM	
<b>in:</b>	Surface of the central cylindrical body ( $cb$ ); BRep of SV ( $sv$ ); $hLayer$ ; $hMax$ ; $hMin$
<b>out:</b>	$c[]$ , set of the outer borders of the layers
<b>local:</b>	$c[]$ <span style="float: right;">▷ List of the output curve</span> $surfaces[]$ $a[]$ <span style="float: right;">▷ List of projected arcs</span> $s[]$ <span style="float: right;">▷ List of segments</span> $surfaces_0 \leftarrow cb$ $i \leftarrow 0$ <span style="float: right;">▷ Layer counter</span>
	▷ Create the first curve and the first arc 1: $c_i \leftarrow \text{BREPINTERSECTION}(sv, surfaces_0)$ 2: $\text{ADDITEM}(c, c_i)$ 3: $circularEdge \leftarrow \text{GETCIRCULAREDGESURFACE}(surfaces_0)$ 4: $projectEdge \leftarrow \text{PROJECTEDGEONPLANE}(circularEdge, xyPlane)$ 5: $centreArc \leftarrow \text{GETARCCENTRE}(projectEdge)$ 6: $a_i \leftarrow \text{GETARC}(c_i, xyPlane, vectorZ, centreArc, projectEdge)$
	7: <b>while</b> $c_i \neq \text{NIL}$ <b>do</b> 8: $surfaces_{i+1} \leftarrow \text{OFFSETSURFACE}(surfaces_i, hLayer)$ 9: $c_{i+1} \leftarrow \text{BREPINTERSECTION}(sv, surfaces_{i+1})$ 10: <b>if</b> $c_{i+1} = \text{NIL}$ <b>then</b> 11: <b>return</b> $c$ <span style="float: right;">▷ The part processing is finished</span> 12: <b>end if</b>
	▷ Create $a_{i+1}$ and $s_{i+1}$ 13: $circularEdge \leftarrow \text{GETCIRCULAREDGESURFACE}(surfaces_{i+1})$ 14: $projectEdge \leftarrow \text{PROJECTEDGEONPLANE}(circularEdge, xyPlane)$ 15: $centreArc \leftarrow \text{GETARCCENTRE}(projectEdge)$ 16: $a_{i+1} \leftarrow \text{GETARC}(c_{i+1}, xyPlane, vectorZ, centreArc, projectEdge)$

```

17:    $s_{i+1} \leftarrow \text{GETARCSEGMENT}(a_{i+1})$ 

▷ Evaluate intersection between  $s_{i+1}$  and  $\text{surfaces}_i$ 
18:    $\text{intersection} \leftarrow \text{BREPCURVEINTERSECTION}(s_{i+1}, \text{surfaces}_i)$ 
19:    $\text{arcMidPoint} \leftarrow \text{GETCURVEMIDPOINT}(a_i)$ 
20:   if  $\text{intersection} = \text{NIL}$  do
21:      $\text{closestPoint} \leftarrow \text{GETCURVECLOSESTPOINT}(\text{arcMidPoint}, s_{i+1})$ 
22:      $d \leftarrow \text{GETDISTANCE}(\text{arcMidPoint}_t, \text{closestPoint})$ 

▷ Planar slicing case
23:     if  $d \geq \text{minH}$ 
24:        $\text{surfaces}_{i+1} \leftarrow \text{CREATESURFACE}(s_{i+1}, \text{vectorZ})$ 
25:        $c_{i+1} \leftarrow \text{BREPINTERSECTION}(sv, \text{surfaces}_{i+1})$ 
26:       while  $c_{i+1} \neq \text{NIL}$  do
27:          $\text{ADDITEM}(c, c_{i+1})$ 
28:          $\text{normalSurface} \leftarrow \text{GETSURFACENORMAL}(\text{surfaces}_{i+1})$ 
29:          $\text{surfaces}_{i+1} \leftarrow \text{MOVESURFACE}(\text{surfaces}_{i+1}, \text{normalSurface} * h\text{Layer})$ 
30:          $c_{i+1} \leftarrow \text{BREPINTERSECTION}(sv, \text{surfaces}_{i+1})$ 
31:         if  $c_{i+1} = \text{NIL}$  then
32:           return  $c$            ▷ The part processing is finished
33:         end if
34:       end while
35:     end if

▷ Cylindrical slicing case
36:     else
37:        $a \leftarrow a_{i+1}$ 
38:        $a_{i+1} \leftarrow \text{COMPUTELAYERARC}(a, \text{arcMidPoint}, h\text{Min})$            ▷  $a$  output
39:
40:        $\text{surfaces}_{i+1} \leftarrow \text{EXTRUDECURVE}(a_{i+1}, \text{vectorZ})$ 
41:        $c_{i+1} \leftarrow \text{BREPINTERSECTION}(sv, \text{surfaces}_{i+1})$ 
42:        $s_{i+1} \leftarrow \text{CREATELINE}(v_1, v_3)$ 
43:        $\text{ADDITEM}(c, c_{i+1})$ 
44:     end if
45:   end if

▷ Cylindrical slicing case
46:   if  $\text{intersection} \neq \text{NIL}$  then
47:      $a \leftarrow a_{i+1}$ 
48:      $a_{i+1} \leftarrow \text{COMPUTELAYERARC}(a, \text{arcMidPoint}, h\text{Min})$            ▷  $a$  output
49:
50:      $\text{surfaces}_{i+1} \leftarrow \text{EXTRUDECURVE}(a_{i+1}, \text{vectorZ})$ 
51:      $c_{i+1} \leftarrow \text{BREPINTERSECTION}(sv, \text{surfaces}_{i+1})$ 
52:      $s_{i+1} \leftarrow \text{CREATELINE}(v_1, v_3)$ 
53:      $\text{ADDITEM}(c, c_{i+1})$ 
54:   end if
55:    $i \leftarrow i + 1$ 
56: end while

```

ALGORITHM 2: COMPUTELAYERARC	
<b>in:</b>	Arc ( <i>arc</i> ), Middle point of the previous arc ( <i>midPoint</i> ), <i>hMin</i>
<b>out:</b>	Arc ( <i>a</i> ), Circular curve ( <i>circle</i> )
<b>local:</b>	$a \leftarrow arc$ <span style="float: right;">▷ Arc</span> $arcMidPoint \leftarrow midPoint$ <span style="float: right;">▷ Middle Point of the</span> previous arc
1:	$closestPoint \leftarrow GETCURVECLOSESTPOINT(arcMidPoint, a)$
2:	$line \leftarrow CREATELINE(arcMidPoint, closestPoint)$
3:	$P_2 \leftarrow EVALUATECURVELLENGTH(line, hMin)$
4:	$P_1 \leftarrow GETARCEEND(a, 0)$
5:	$P_3 \leftarrow GETARCEEND(a, 1)$
6:	$a \leftarrow CREATEARC3PT(P_1, P_2, P_3)$
7:	<b>return</b> <i>a</i>

**Author contribution** All authors contributed to the study's conception and design. Jacopo Lettori and Roberto Raffaelli performed material preparation, data collection, and analysis. Jacopo Lettori wrote the first draft of the manuscript, and all authors commented on previous versions. All authors read and approved the final manuscript.

**Data availability** Not applicable.

**Code availability** Not applicable.

## Declarations

**Ethics approval** Not applicable.

**Consent to participate** Not applicable.

**Consent for publication** Not applicable.

**Competing interests** The authors declare no competing interests.

## References

- Qin Y, Qi Q, Scott PJ, Jiang X (2019) Determination of optimal build orientation for additive manufacturing using Muirhead mean and prioritised average operators. *J Intell Manuf* 30:3015–2034. <https://doi.org/10.1007/s10845-019-01497-6>
- Choi SH, Kwok KT (2002) A tolerant slicing algorithm for layered manufacturing. *Rapid Prototyp J* 8:161–179. <https://doi.org/10.1108/13552540210430997>
- Minetto R, Volpato N, Stolfi J et al (2017) An optimal algorithm for 3D triangle mesh slicing. *CAD Comput Aided Des* 92:1–10. <https://doi.org/10.1016/j.cad.2017.07.001>
- Lettori J, Raffaelli R, Bilancia P et al (2022) A review of geometry representation and processing methods for cartesian and multi-axial robot-based additive manufacturing. *Int J Adv Manuf Technol* 123:3767–3794. <https://doi.org/10.1007/s00170-022-10432-8>
- Sabourin E, Houser SA, Bøhn JH (1996) Adaptive slicing using stepwise uniform refinement. *Rapid Prototyp J* 2:20–26. <https://doi.org/10.1108/13552549610153370>
- Gohari H, Kishawy H, Barari A (2021) Adaptive variable layer thickness and perimetral offset planning for layer-based additive manufacturing processes. *Int J Comput Integr Manuf* 34:964–974. <https://doi.org/10.1080/0951192X.2021.1946854>
- Mao H, Kwok TH, Chen Y, Wang CCL (2019) Adaptive slicing based on efficient profile analysis. *CAD Comput Aided Des* 107:89–101. <https://doi.org/10.1016/j.cad.2018.09.006>
- Jiang J, Xu X, Stringer J (2018) Support structures for additive manufacturing: a review. *J Manuf Mater Process* 2:64. <https://doi.org/10.3390/jmmp2040064>
- Rauch M, Hascoet J-Y, Querard V (2021) A multi-axis tool path generation approach for thin wall structures made with WAAM. *J Manuf Mater Process* 5(4):128. <https://doi.org/10.3390/jmmp5040128>
- Wu C, Dai C, Fang G et al (2020) General support-effective decomposition for multi-directional 3-D printing. *IEEE Trans Autom Sci Eng* 17:599–610. <https://doi.org/10.1109/TASE.2019.2938219>
- Jiang J, Newman ST, Zhong RY (2021) A review of multiple degrees of freedom for additive manufacturing machines. *Int J Comput Integr Manuf* 34:195–211. <https://doi.org/10.1080/0951192X.2020.1858510>
- Lettori J, Raffaelli R, Borsato M, et al (2022) An approach for volume decomposition in robot-based additive manufacturing. *D:313–317*. <https://doi.org/10.14733/cadconf.2022.313-317>
- Xie F, Jing X, Zhang C et al (2022) Volume decomposition for multi-axis support-free and gouging-free printing based on ellipsoidal slicing. *Comput Des* 143:103135. <https://doi.org/10.1016/j.cad.2021.103135>

14. Chen L, Chung MF, Tian Y et al (2019) Variable-depth curved layer fused deposition modeling of thin-shells. *Robot Comput Integr Manuf* 57:422–434. <https://doi.org/10.1016/j.rcim.2018.12.016>
15. Zhang J, Liou F (2004) Adaptive slicing for a multi-axis laser aided manufacturing process. *J Mech Des Trans ASME* 126:254–261. <https://doi.org/10.1115/1.1649966>
16. Lettori J, Raffaelli R, Borsato M, et al (2024) Non-uniform planar slicing for robot-based additive manufacturing. 21:237–241. <https://doi.org/10.14733/cadconf.2023.237-241>
17. Huang B, Singamneni SB (2015) Curved layer adaptive slicing (CLAS) for fused deposition modelling. *Rapid Prototyp J* 21:354–367. <https://doi.org/10.1108/RPJ-06-2013-0059>
18. Wang X, Chen L, Lau T-Y, Tang K (2020) A skeleton-based process planning framework for support-free 3+2-axis printing of multi-branch freeform parts. *Int J Adv Manuf Technol* 110:327–350. <https://doi.org/10.1007/s00170-020-05790-0>
19. Ruan J, Sparks TE, Panackal A et al (2007) Automated slicing for a multi-axis metal deposition system. *J Manuf Sci Eng Trans ASME* 129:303–310. <https://doi.org/10.1115/1.2673492>
20. Kalmanovich G (1996) “Curved-layer” laminated object manufacturing. In: 1996 International Solid Freeform Fabrication Symposium, pp 273–280. <http://hdl.handle.net/2152/70244>
21. Kerschbaumer M, Ernst G, O’Leary P (2005) Tool path generation for 3D laser cladding using adaptive slicing technology. 24th Int Congr Appl Lasers Electro-Optics ICALAO 2005 - Congr Proc 604:310–319. <https://doi.org/10.2351/1.5060506>
22. Zhao G, Ma G, Feng J, Xiao W (2018) Nonplanar slicing and path generation methods for robotic additive manufacturing. *Int J Adv Manuf Technol* 96:3149–3159. <https://doi.org/10.1007/s00170-018-1772-9>
23. Dai F, Zhang H, Li R (2020) Process planning based on cylindrical or conical surfaces for five-axis wire and arc additive manufacturing. *Rapid Prototyp J*. <https://doi.org/10.1108/RPJ-01-2020-0001>
24. Ding Y, Dwivedi R, Kovacevic R (2017) Process planning for 8-axis robotized laser-based direct metal deposition system: a case on building revolved part. *Robot Comput Integr Manuf* 44:67–76. <https://doi.org/10.1016/j.rcim.2016.08.008>
25. Xiao W, Huan J (2012) Redundancy and optimization of a 6R robot for five-axis milling applications: singularity, joint limits and collision. *Prod Eng* 6:287–296. <https://doi.org/10.1007/s11740-012-0362-1>
26. Bigliardi M, Bilancia P, Raffaelli R, et al (2022) Path approximation strategies for robot manufacturing: a preliminary experimental evaluation. In: Advances on mechanics, design engineering and manufacturing IV: Proceedings of the International Joint Conference on Mechanics, Design Engineering & Advanced Manufacturing, JCM 2022, June 1–3, 2022, Ischia, Italy. Springer, 380–389
27. Tajima S, Iwamoto S, Yoshioka H (2021) Kinematic tool-path smoothing for 6-axis industrial machining robots. *Int J Autom Technol* 15:621–630. <https://doi.org/10.20965/ijat.2021.p0621>
28. Li G, Liu H, Liu S, Xiao J (2022) A general C2 continuous tool-path corner smoothing method for a 5-DOF hybrid robot. *Mech Mach Theory* 169:104640. <https://doi.org/10.1016/j.mechmachtheory.2021.104640>
29. Ding D, Pan Z, Cuiuri D et al (2016) Automatic multi-direction slicing algorithms for wire based additive manufacturing. *Robot Comput Integr Manuf* 37:139–150. <https://doi.org/10.1016/j.rcim.2015.09.002>
30. Rhinoceros 3D. <https://www.rhino3d.com/>
31. RoboDK. <https://robodk.com/>
32. Fortunato GM, Nicoletta M, Batoni E, et al (2023) A fully automatic non-planar slicing algorithm for the additive manufacturing of complex geometries. *Addit Manuf* 103541. <https://doi.org/10.1016/j.addma.2023.103541>
33. Huang B, Singamneni S (2014) Curved layer fused deposition modeling with varying raster orientations. *Appl Mech Mater* 446–447:263–269. <https://doi.org/10.4028/www.scientific.net/AMM.446-447.263>
34. Zhao D, Guo W (2020) Mixed-layer adaptive slicing for robotic additive manufacturing (AM) based on decomposing and regrouping. *J Intell Manuf* 31:985–1002. <https://doi.org/10.1007/s10845-019-01490-z>
35. Dai C, Wang CCL, Wu C et al (2018) Support-free volume printing by multi-axis motion. *ACM Trans Graph* 37:1–14. <https://doi.org/10.1145/3197517.3201342>
36. Ahlers D, Wasserfall F, Hendrich N, Zhang J (2019) 3D printing of nonplanar layers for smooth surface generation. In: 2019 IEEE 15th international conference on automation science and engineering (CASE). IEEE, 1737–1743
37. Llewellyn-Jones T, Allen R, Trask R (2016) Curved layer fused filament fabrication using automated toolpath generation. *3D Print Addit Manuf* 3:236–243. <https://doi.org/10.1089/3dp.2016.0033>
38. Rosa F, Graziosi S (2019) A parametric and adaptive slicing (PAS) technique: general method and experimental validation. *Rapid Prototyp J* 25:126–142. <https://doi.org/10.1108/RPJ-11-2016-0184>
39. Etienne J, Ray N, Panozzo D et al (2019) Curvislicer: slightly curved slicing for 3-axis printers. *ACM Trans Graph* 38:1–11. <https://doi.org/10.1145/3306346.3323022>
40. Shan Y, Shui Y, Hua J, Mao H (2023) Additive manufacturing of non-planar layers using isothermal surface slicing. *J Manuf Process* 86:326–335. <https://doi.org/10.1016/j.jmapro.2022.12.054>
41. Williams SW, Martina F (2015) Wire+arc additive manufacturing vs. traditional machining from solid: a cost comparison. Technical Report, Cranfield University
42. Lockett H, Ding J, Williams S, Martina F (2017) Design for wire + arc additive manufacture: design rules and build orientation selection. *J Eng Des* 28:568–598. <https://doi.org/10.1080/09544828.2017.1365826>
43. Dwivedi R, Kovacevic R (2004) Automated torch path planning using polygon subdivision for solid freeform fabrication based on welding. *J Manuf Syst* 23:278–291. [https://doi.org/10.1016/S0278-6125\(04\)80040-2](https://doi.org/10.1016/S0278-6125(04)80040-2)
44. Ding Y, Akbari M, Kovacevic R (2018) Process planning for laser wire-feed metal additive manufacturing system. *Int J Adv Manuf Technol* 95:355–365. <https://doi.org/10.1007/s00170-017-1179-z>
45. Yigit IE, Khan SA, Lazoglu I (2022) Robotic additive turning with a novel cylindrical slicing method. *Int J Adv Manuf Technol* 119:7641–7651. <https://doi.org/10.1007/s00170-021-08567-1>
46. Wang R, Zhang H, Gui-Lan W, Zhao X (2019) Cylindrical slicing and path planning of propeller in wire and arc additive manufacturing. *Rapid Prototyp J*. <https://doi.org/10.1108/RPJ-02-2019-0035>
47. He T, Yu S, Shi Y, Dai Y (2019) High-accuracy and high-performance WAAM propeller manufacture by cylindrical surface slicing method. *Int J Adv Manuf Technol* 105:4773–4782. <https://doi.org/10.1007/s00170-019-04558-5>
48. Dharmawan AG, Soh GS (2022) A cylindrical path planning approach for additive manufacturing of revolved components. *Mater Sci Add Manuf* 1. <https://doi.org/10.18063/msam.v1i1.3>
49. Dai F, Zhang S, Li R, Zhang H (2021) Multi-axis wire and arc additive manufacturing for overhangs based on conical substrates. *Rapid Prototyp J*. <https://doi.org/10.1108/RPJ-12-2020-0300>
50. Lettori J, Raffaelli R, Borsato M, et al (2023) Empirical characterization of track dimensions for CMT-based WAAM processes. In: Silva FJG, Ferreira LP, Sà JC, et al (eds) Flexible automation and intelligent manufacturing: establishing bridges for more sustainable manufacturing systems. Springer, Cham

51. Jafari D, Vaneker THJ, Gibson I (2021) Wire and arc additive manufacturing: opportunities and challenges to control the quality and accuracy of manufactured parts. *Mater Des* 202:109471. <https://doi.org/10.1016/j.matdes.2021.109471>
52. Selvi S, Vishvaksean A, Rajasekar E (2018) Cold metal transfer (CMT) technology-an overview. *Def Technol* 14:28–44. <https://doi.org/10.1016/j.dt.2017.08.002>
53. Yuan L, Pan Z, Ding D et al (2021) Fabrication of metallic parts with overhanging structures using the robotic wire arc additive manufacturing. *J Manuf Process* 63:24–34. <https://doi.org/10.1016/j.jmapro.2020.03.018>
54. Raffaelli R, Mengoni M, Germani M, Mandorli F (2009) An approach to support the implementation of product configuration

tools. In: *International Design Engineering Technical Conferences and Computers and Information in Engineering Conference*. ASME, San Diego, CA, pp 559–570. <https://doi.org/10.1115/DETC2009-86752>

**Publisher's Note** Springer Nature remains neutral with regard to jurisdictional claims in published maps and institutional affiliations.

Springer Nature or its licensor (e.g. a society or other partner) holds exclusive rights to this article under a publishing agreement with the author(s) or other rightsholder(s); author self-archiving of the accepted manuscript version of this article is solely governed by the terms of such publishing agreement and applicable law.